Macromolecules

pubs.acs.org/Macromolecules

Article

Machine Learning Approach to Characterize the Adhesive and Mechanical Properties of Soft Polymers Using PeakForce Tapping AFM

Bahram Rajabifar, Gregory F. Meyers, Ryan Wagner, and Arvind Raman*

Cite This: *Macromolecules* 2022, 55, 8731−8740

Read Online

ACCESS | Metrics & More | Article Recommendations | Supporting Information

ABSTRACT: We develop an algorithm based on the enhanced Attard's model (EAM) to simulate PeakForce tapping (PFT) atomic force microscopy (AFM) on soft adhesive polymers. The simulations enhance our understanding of microcantilever−surface interactions, predict surface dynamics, and illustrate the role of viscoelasticity and adhesion on PFT AFM observables. Behaviors predicted by the developed algorithm cannot be fully reproduced with alternative contact mechanics models. In the second part of this study, we utilize the output of our PFT AFM simulations to train a data analytics approach that quantitatively estimates a surface's viscoelastic and adhesive properties from experimentally acquired PFT AFM data. We demonstrate the performance of a machine learning (ML) algorithm to estimate the properties of three elastomer grades with different nominal stiffnesses. The properties extracted from the PFT AFM data using the ML algorithm agree well with the bulk properties of these polymers.

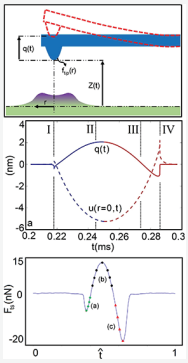

INTRODUCTION

Current atomic force microscopy (AFM) operational modes with appropriate modifications are capable of reconstructing the complete tip−surface interaction forces to estimate a sample's nanoscale mechanical properties.[1] Force volume mapping (FVM),[2] contact resonance AFM (CR),[3−5] bimodal AFM,[6] PeakForce Tapping (PFT),[7] quantitative imaging (QI),[8] tapping mode AFM (TM),[9] and fast force mapping (FFM)[10] are examples of operational modes that provide a pathway to obtain force−distance curves. These modes differ in terms of the excitation frequency utilized (resonant or sub-resonant), acquisition speed, instrument control loops, and recorded observables.[8,10,11] In the sub-resonance FVM-like modes, either the microcantilever base or the sample is excited through a periodic (not necessarily sinusoidal) displacement waveform with a frequency, ω_z, far below the fundamental resonance of the microcantilever, ω.[12] Both the tip deflection, $q(t)$, and the relative sample position, $Z(t)$, are recorded during each oscillation cycle (Figure 1a). The tip deflection is translated into the tip−surface interaction force, F_{ts}, with a point mass model using microcantilever stiffness k,[13] as shown in Figure 1b. At each image pixel, the control loop adjusts the average Z position to maintain a specified imaging setpoint. This enables simultaneous extraction of surface topography. The image acquisition rate in these sub-resonance modes is generally slower than in resonant modes. However, these sub-resonance modes enable simpler measurement architectures for extracting the tip−sample interaction force.

PFT AFM is a mode offered on Bruker (Santa Barbara, CA) AFMs in which the Z position is modulated by a prescribed sinusoidal waveform ($\omega_z \ll \omega$) which can be expressed as

$$Z(t) = Z_0 + A_Z \cos(\omega_Z t) \quad (1)$$

where Z_0 is the average tip distance from the surface and A_z is the oscillation amplitude of the microcantilever base. In this study, we assume the Z modulation is applied through oscillating the microcantilever base with respect to the stationary sample stage. However, if the instrument is designed based on the scanner movement, A_z will be defined as the scanner oscillation amplitude, and the rest of the following derivation remains the same. Z_0 is adjusted by the controller to maintain a set peak interaction force between the tip and the surface during imaging. The smooth sinusoidal Z velocity profile in PFT AFM prevents common artifacts associated with triangular Z modulation such as unwanted piezoelectric tube oscillations and coupling to higher harmonics. This enables PFT AFM to simultaneously map topography and acquire force curves at higher imaging speeds and with better peak force control than other FVM methods. The schematic shown in Figure 2 shows the tip deflection and surface deformation

Received: January 20, 2022
Revised: August 16, 2022
Published: September 21, 2022

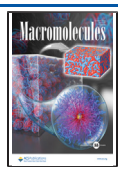

https://doi.org/10.1021/acs.macromol.2c00147
Macromolecules 2022, 55, 8731−8740

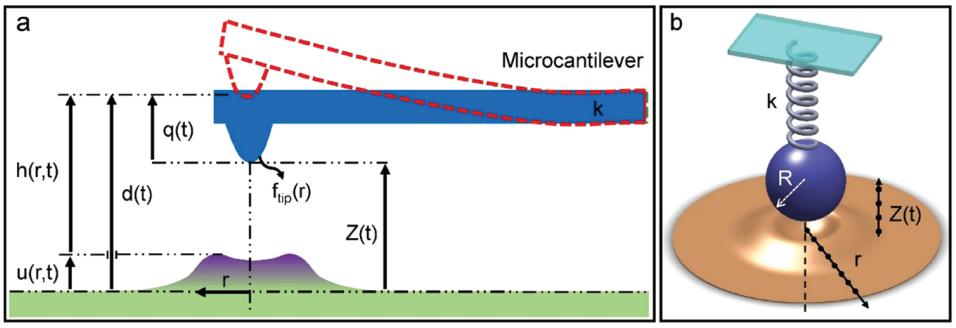

Figure 1. (a) Schematic of an interacting AFM microcantilever tip and a surface in FVM-like AFM operational modes is illustrated, and the relevant parameters are specified: the tip−surface distance $Z(t)$, tip deflection $q(t)$, surface deformation $u(r, t)$, and axisymmetric tip profile $f_{tip}(r)$. The other parameters shown in the figure can be defined based on $Z(t)$, $q(t)$, $u(r, t)$, and $f_{tip}(r)$ as follows: $d(t) = Z(t) + q(t)$, $h(r, t) = d(t) + f_{tip}(r) - u(r, t)$. (b) Equivalent point mass model representation for a rectangular microcantilever excited at a sub-resonant frequency.

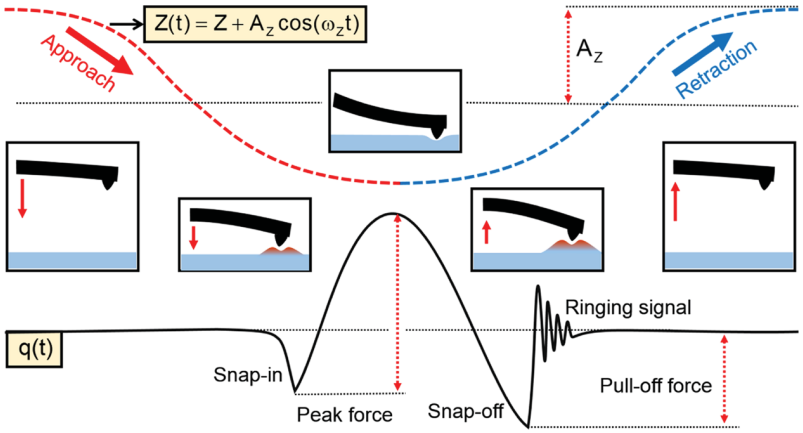

Figure 2. Schematic of PFT AFM on a soft sample. The dashed red-blue curve shows the trajectory of the microcantilever base during a cycle (eq 1). The black solid curve represents the tip deflection (q) during a cycle.

time history during a PFT AFM cycle on a compliant surface. At the end stages of each cycle, when the retracting tip fully detaches from the surface, the conversion of potential to kinetic energy of the microcantilever leads to its freely ringing without interacting with the surface. This high-frequency segment of the output signal is filtered out in PFT through averaging over a set of force curves at each image pixel and the use of denoising algorithms.[14]

Despite instrumentation enhancements in PFT AFM that facilitate high-quality experimental data, rigorous methodologies that link the acquired force curves to nanoscale mechanical properties of soft, viscoelastic, and adhesive polymers are not yet established. This gap is partially due to the more complex response to external time-varying loads of viscoelastic materials with surface forces. In contrast with elastic materials, the force-deformation relation for viscoelastic materials not only depends on the amount of deformation but also is contingent on the deformation history and its rate. Models that systematically include the 3D viscoelastic properties within a continuum mechanics framework make more reliable and accurate predictions than models that introduce viscoelastic behavior with *ad hoc* addition of a viscoelastic element to elastic contact mechanic models.[15] These *ad hoc* models usually proceed by combining a Kelvin−Voigt (KV) viscoelastic element in parallel with an elastic contact model, such as Hertz.[16] In contrast, the continuum mechanics-based models, such as the one proposed by Ting,[17] expand the elastic contact models to capture the complex response of viscoelastic materials through the use of the convolution theorem.[18] However, these models do not apply to adhesive surfaces, and the complexity of the continuum mechanics-based models does not allow the derivation of a closed-form solution for the force−displacement problem. This lack of a closed-form solution complicates their use to estimate the viscoelastic properties of the materials based on the associated acquired AFM observables. Furthermore, the required computational cost for simulating the AFM modes using continuum mechanics-based models is much higher than their elastic or *ad hoc* viscoelastic counterparts.

The continuum mechanics-based contact model proposed by Attard[19,20] is arguably the most comprehensive and rigorous model to capture the physics of interaction on adhesive viscoelastic samples. In prior work, we implemented three key enabling strategies on Attard's model to enhance its computational part and make it faster and more robust.[21] These strategies are (a) using a set of optimized orthogonal basis functions instead of the computationally expensive radial discretization technique of the original Attard's model; (b) solving the model's governing ordinary differential equations (ODEs) using multistep Adams−Bashforth methods, and (c) facilitating the explicit solution of the ODEs of the model by rearranging the original formalism. The resultant enhanced Attard's model (EAM) is 3+ orders of magnitude faster, more stable, and equally accurate in comparison with the original Attard's model. EAM enables fast and rigorous calculation of the tip−surface interaction force on viscoelastic samples with

https://doi.org/10.1021/acs.macromol.2c00147
Macromolecules 2022, 55, 8731−8740

surface forces. EAM allows incorporating arbitrary surface long-range forces and linear viscoelasticity constitutive models. Nonetheless, linking the AFM observables to the mechanical properties of the surface using EAM is not straightforward. The complexity is partially due to how the model's solution is structured. Attard's solution for the contact problem between a compliant surface and a rigid tip is a multistep procedure. First, based on the relative distance between the tip and the undeformed surface at each timestep the solution of the model's governing ODEs yields the surface deformation velocity at each radial distance. Second, the deformed surface profile is predicted and reconstructed. The force between the tip and deformed surface at each radial location is computed based on the tip−surface distance using the employed potential model. Finally, the total interaction force is calculated based on integration of the tip−surface pressure over the whole computational domain. When using this multistep procedure, it is not possible to analytically solve the inverse problem to link the tip−surface force to the material surface viscoelastic and adhesive properties.

In this work, we first develop an algorithm to predict PFT force curves with a known set of operating conditions, microcantilever parameters, and material viscoelastic and adhesive properties. The algorithm adopts EAM to model the tip−surface interactions when performing PFT AFM on viscoelastic adhesive surfaces.[21] The algorithm is then employed to conduct a parametric study to predict variations in force−distance curves due to changes in PFT AFM operational parameters, microcantilever parameters, and surface properties. In the second part of this work, we examine using a machine learning (ML) algorithm to estimate the viscoelastic and adhesive properties of the sample based on observed PFT AFM force curves. We use simulations of PFT AFM experiments over a range of input parameters to generate a data set to train and test the employed ML algorithm. Finally, we implement the ML algorithm on acquired experimental PFT data of a set of polymer samples. The estimated surface mechanical properties by the ML method agree well with the sample's macroscale properties.

THEORY

In PFT AFM, the interaction between the tip of a microcantilever and a surface is monitored and recorded while the Z distance of the microcantilever is modulated by a sinusoidal waveform: eq 1. The absolute deflection of the microcantilever at a distance x from the base of the microcantilever at time t, $w(x, t)$, is composed of two components: $Z(t)$, and $q_b(x, t)$, which is the transverse deflection of the beam in the noninertial frame attached to the base

$$w(x, t) = Z(t) + q_b(x, t) \tag{2}$$

We model the deflection of the microcantilever in PFT AFM with the partial differential equation (PDE) of Euler−Bernoulli beam theory. Since $\bar{\omega} = \omega/\omega_z \gg 1$ in PFT AFM (sub-resonance), the effect of the interference between the higher harmonics of the drive frequency and the first eigenfrequency of the microcantilever can be safely ignored. Therefore, the inertial and damping terms of the beam PDEs become negligible, and the steady-state solution of the microcantilever motion can be approximated as follows

$$k\,q(t) \approx F_{ts}(t) \tag{3}$$

where k is the effective stiffness of the microcantilever and $q(t)$ is the tip deflection at time t. eq 3 can be represented as an equivalent point mass model shown in Figure 1b. Transient phenomena such as microcantilever ringing during retraction cannot be captured using the quasistatic solutions to Euler−Bernoulli beam theory.

We use EAM[21] to calculate F_{ts} in eq 3, and we model the surface viscoelasticity and tip−surface interaction by the standard linear solid (SLS) model and Lennard-Jones (LJ) equation,[20] respectively. The creep compliance function, $J(t)$, of an SLS viscoelastic element is

$$J(t) = \frac{1}{E_\infty} + \frac{E_\infty - E_0}{E_0 E_\infty} e^{-t/\tau} \tag{4}$$

where, τ, E_∞, and E_0 are retardation (creep) time and long- and short-term moduli of the surface, respectively. Alternative viscoelastic constitutive models can be embedded in EAM so long as their creep compliance function can be specified. According to the LJ pressure equation, the interaction force per unit area (pressure) between two parallel and infinite surfaces with distance h is expressed as follows

$$p(h) = \frac{H}{6\pi h^3}\left(\frac{z_0^6}{h^6} - 1\right) \tag{5}$$

where Z_0 and H are the intermolecular equilibrium distance and Hamaker constant of interacting surfaces, respectively.

In EAM, the deformed surface profile, $u(r, t)$, is numerically calculated from the differential equations governing the viscoelastic and adhesive interactions between the tip and the surface. The total tip−sample interaction force at each timestep, $F_{ts}(t)$, is recovered from integrating the contact pressure $p(h(r, t))$ over the entire computational domain. The details of this process are described in a Supporting Information Section and in prior publications.[20]

Figure 3 illustrates the flowchart of the algorithm used to solve $F_{ts}(t)$, given the motion of the base of the microcantilever and the properties of the sample (i.e., the forward problem). The algorithm starts with a guessed tip deflection for each timestep, q_g, which is then progressively adjusted by the algorithm until $F_{ts}(t)$ calculated with EAM equals $k \times q_g$ for that timestep, as in eq 3. This procedure continues for all timesteps of an oscillation cycle to complete the force curve prediction process. The subscript "g" in Figure 3 denotes a guessed value for a parameter.

Forward Problem. In PFT AFM the forward problem is the prediction of the tip−sample interaction force, the tip trajectory, and the surface dynamics, given the properties of the sample, the properties of the microcantilever, and the AFM operating conditions. Figure 4 illustrates using the forward problem algorithm to simulate a single PFT AFM cycle on an elastomer sample. The utilized elastomer viscoelastic properties and the PFT operational parameters are listed in column "*" of Table 1. The predicted time-resolved $u(r = 0, t)$ and $q(t)$ are illustrated in Figure 4a, and $F_{ts}(t)$ vs d is shown in Figure 4b. The tip−surface position and pressure distribution over the computational domain for the labeled timestamps in Figure 4a (I, II, III, and IV) are shown in Figure 4c−f and g−j, respectively.

During the tip approach, the long-range attractive forces between the axisymmetric rigid tip and the surface cause the microcantilever to deflect down toward the surface (Figure 4a). Simultaneously, on the sample side, the attractive forces

https://doi.org/10.1021/acs.macromol.2c00147
Macromolecules 2022, 55, 8731−8740

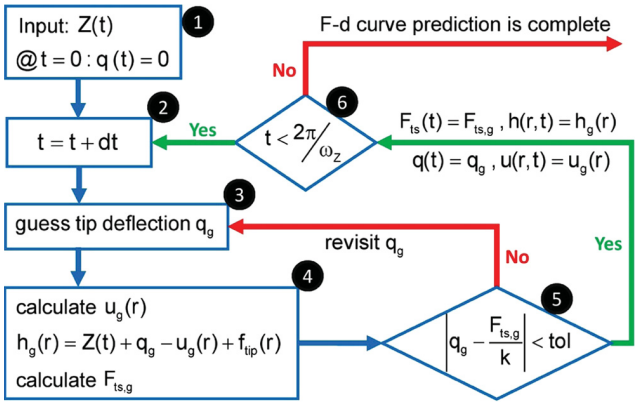

Figure 3. Algorithm utilized in this work for predicting the $F-d$ curve in PFT AFM. The process starts with known $Z(t)$ for the whole cycle and a guessed tip deflection (q_g) for timestep "$t = dt$" (steps1 and 2). Since "dt" is selected to be very small, the tip deflection at each timestep is very close to previously recorded $q(t)$. We continue the process (step 4) using EAM to compute the associated surface deformation $u_g(r)$ and tip−surface interaction force ($F_{ts,g}$). Then, we check if the guessed/derived (q_g, $F_{ts,g}$) set satisfies eq 3 (step 5) considering the acceptable tolerance (tol). If not, we revisit the q_g assumption and repeat the process for the current timestep (step 3). If yes, we record all of the guessed/derived parameters as final and then repeat the same process for the next timestep (step 2). This will continue until the data for the whole cycle is recorded (step 6). The axisymmetric tip profile is defined by $f_{tip}(r)$.

between the tip and sample cause the surface to gradually rise upward from its initial flat state. Eventually, when the gradient of F_{ts} exceeds the microcantilever stiffness, k, the tip of the deflected down microcantilever and the bulged surface meet each other above the undeformed surface level through a rapid unstable phenomenon called "snap-in" (also known as jump to contact). The snap-in instance of the cycle is labeled as I in Figure 4a, and its associated surface deformation, $u(r, t)$, and the pressure distribution over the computational domain, $p(r, t)$, are shown in Figure 4c,g, respectively.

By further approaching, the total interaction force between the tip and the surface gradually switches to net repulsive, and the microcantilever deflects upward. The tip continues to indent the surface until $F_{ts}(t)$ reaches the peak force setpoint, and then the microcantilever begins to retract. Instances labeled as II and III in Figure 4a, with their associated $u(r, t)$ shown in Figure 4d,e, and $p(r, t)$ shown in Figure 4h,i, respectively, represent this part of the cycle. As seen in Figure 4h,i, while the total tip−surface interaction is repulsive, the predicted pressure distribution over the contact region by the algorithm includes a repulsive pressure near the center of the tip surrounded by regions with attractive pressures.

During retraction, the central repulsive tip−surface interaction region gradually shrinks, and the attractive tip−surface interaction region expands. Interestingly, $F_{ts}(t) = 0$ either during approach or retraction does not indicate any interaction between the tip and the surface. Rather, $F_{ts}(t) = 0$ means that the tip is under both repulsive and attractive force components that are equal in magnitude and cancel out. As shown in Figure 4a, when $F_{ts}(t) = 0$ during retraction, the surface is still below the undeformed level ($u(r = 0, t) < 0$), and the viscoelastic material needs more time to return to its undeformed equilibrium. If there is no effective attractive force between the tip and sample, the retracting tip leaves the yet indented surface when $F_{ts}(t) = 0$. However, when the material is soft and the long-range attractive forces are significant, the surface forms a meniscus around the retracting tip profile, and detachment occurs through a gradual "peeling off" process. In this process, the outermost areas of the contact region on the surface gradually detach from the tip until it fully separates through another unstable phenomenon called "snap-off" (labeled as IV in Figure 4a). The associated $u(r, t)$ and $p(r,$

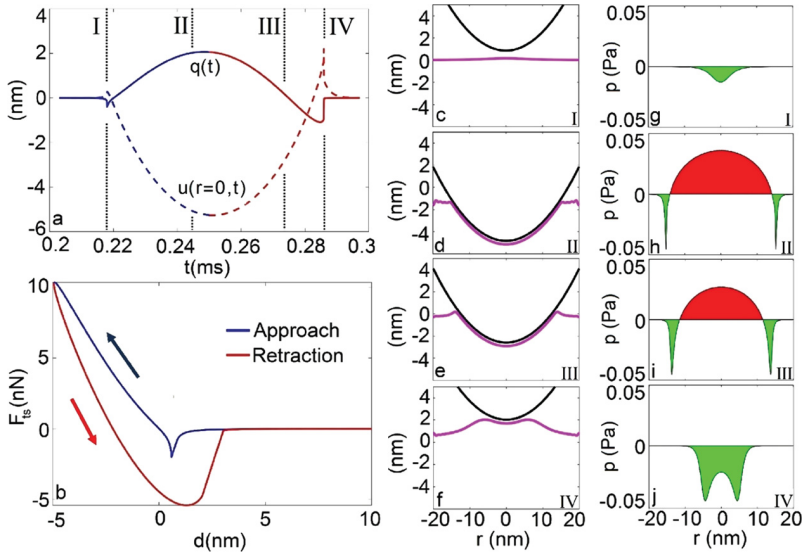

Figure 4. Simulation results for a single-cycle of PFT AFM on an elastomer sample using the developed algorithm. (a): time-resolved tip deflection and surface deformation at $r = 0$ (dashed line); (b): predicted $F-d$ curve. The approach and retraction phases of the interaction cycle are shown in blue and red in panels (a) and (b), respectively. Four instances of the interaction time representing snap-in, indentation, $F_{ts}(t) \approx 0$, and snap-off are marked with vertical dotted lines and labeled as I, II, III, and IV in panel (a), respectively. The associated surface deformation and pressure distributions over the contact region for these instances are shown in panels (c)−(f) and panels (g)−(j), respectively. The instant label for each of these graphs is specified at the bottom-right of subfigures (c)−(f). The green and red areas in subfigures (g)−(j) represent attractive and repulsive interaction pressures, respectively.

https://doi.org/10.1021/acs.macromol.2c00147
Macromolecules 2022, 55, 8731−8740

Table 1. Operational Parameters and Material Properties Used in Simulations for Visualizing the Microcantilever−Sample Interaction in the Parametric Study[a]

	*	a	b	c	d	e	f	g	h	i
R (nm)	30	30	30	30	30	30	30		30	30
k (N/m)	5	5	5	5	5	5		5	5	5
f (kHz)	2	2	2	2	2	2	2	2	2	
A_Z (nm)	100	100	100	100	100	100	100	100		100
E_0 (GPa)	1	1	1	1			1	1	1	1
E_∞ (GPa)	0.1	0.1	0.1		0.1		0.1	0.1	0.1	0.1
H (10^{-20} J)	8		8	8	8	8	8	8	8	8
z_0 (nm)	0.31	0.31		0.31	0.31	0.31	0.31	0.31	0.31	0.31

[a]The colored cells are the parameters whose values are varied over the range specified in the subfigure legends in Figure 5. *R*, *k*, and *f* are the tip radius, stiffness of the microcantilever, and its excitation frequency, respectively. A_z is the *Z* oscillation amplitude. E_0, E_∞, *H*, and z_0 are short-term modulus, long term modulus, Hamaker constant, and equilibrium distance between tip and surface molecules, respectively.

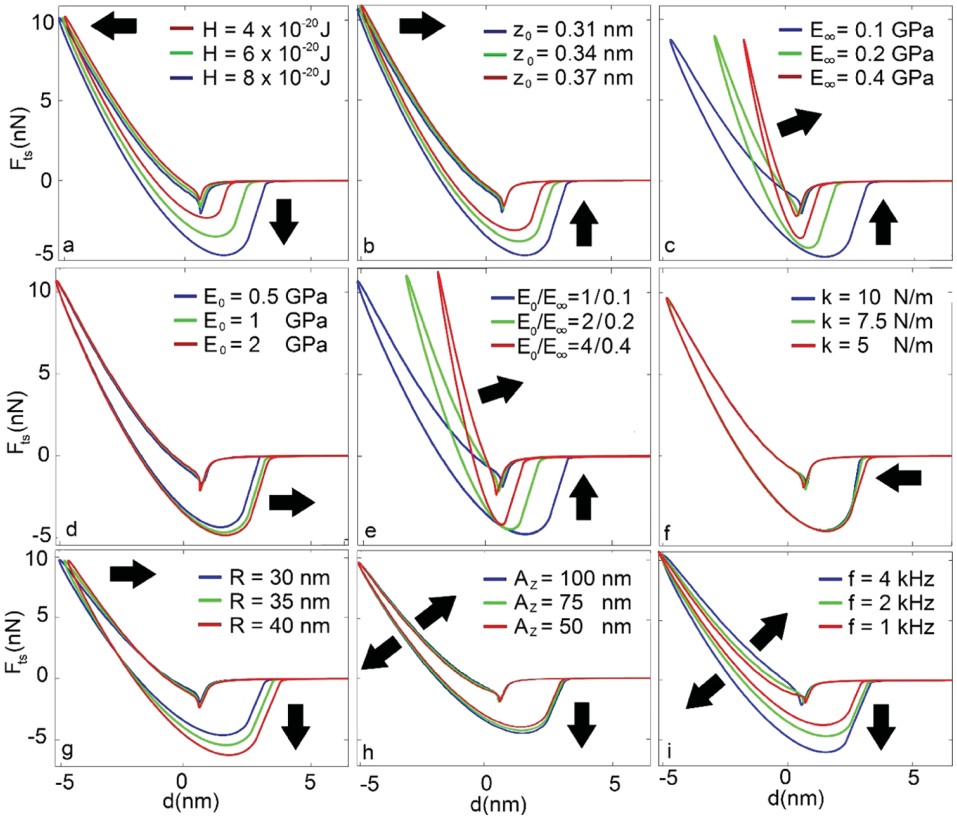

Figure 5. Predicted variation in *F*−*d* curves when the operational parameters and surface viscoelastic and adhesive properties are changed. Each graph (except (e)) changes only one parameter as specified in the legend, and other surface properties or operational parameters remain identical. At panel (e), both E_0 and E_∞ are changed, while the E_∞/E_0 ratio remains constant. Full input parameters used for each set of simulations are listed in Table 1. For all simulations, $\tau = 1$ μs. The peak tip−surface interaction force is the same for all conducted simulations. The model maintains peak force via tuning the average tip−surface distance (Z_0 in eq 1). Arrows indicate changes in the *F*−*d* curves from increasing the studied parameter in each subfigure.

https://doi.org/10.1021/acs.macromol.2c00147
Macromolecules 2022, 55, 8731−8740

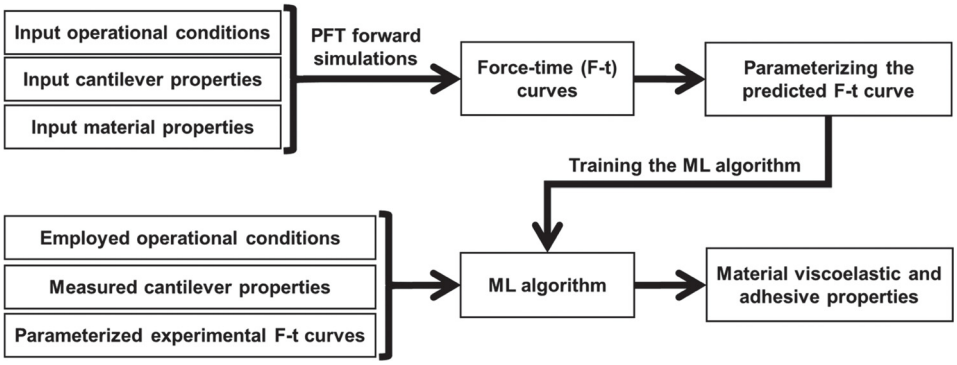

Figure 6. Flowchart illustrates the two-step method used to estimate a material's viscoelastic and adhesive properties based on an experimentally acquired PFT $F-t$ curve. The procedure employs a machine learning algorithm that is trained by a data set of the forward simulation results.

t) for this instance are shown in Figure 4f,j, respectively. The position of the surface at which the tip snaps off during the retraction phase depends on various parameters such as the adhesion of the surface, tip radius, maximum indentation depth, contact time, and viscoelastic properties of the sample. The value of $F_{ts}(t)$ when the tip snaps off is called the "pull-off force" and is traditionally perceived as the adhesion of the surface. When the final detachment happens, the surface relaxes to its original state over its characteristic timescale. This illustrates the adhesion-related energy loss mechanism when conducting AFM on soft viscoelastic polymers in which the attractive tip−sample forces cause the microcantilever energy to be used to overcome the return speed reduction of the deformed area. In this work, we assume the surface will be provided enough chance to return to its original state before being struck in the subsequent PFT cycle.

The full set of predictions for the microcantilever-sample interactions in PFT AFM using EAM in the implemented algorithm cannot be fully reproduced using any of the classical contact models such as Hertz,[16] JKR (Johnson, Kendall, and Roberts),[22] DMT (Derjaguin, Muller, and Toporov),[23] Ting's model,[17] or *ad hoc* viscoelasticity contact models. The algorithm enables a realistic understanding of how the cantilever and the surface behave during a PFT interaction cycle. The tip−surface attractive forces lead to adhesion-induced energy dissipation (hysteresis) when conducting PFT on compliant polymers. In addition, the model predictions show that the pull-off force is a sole function of not only the surface adhesion but also the surface mechanical properties. Therefore, judgment on the tip−surface adhesion of two adjacent polymeric domains of a sample based on the observed pull-off force is valid only if the mechanical properties of the domains are comparable. The model can rigorously capture the instantaneous stiffness difference in the contact radius at each timestep during the interaction cycle based on their distance from the central contact line (r). This difference originates from the dissimilar interaction cycles for the regions with different r values.

To understand how predictions of our algorithm are affected by changes in input parameters, we conducted a series of parametric studies. In Figure 5, the effect of varying selected microcantilever parameters, surface properties, or operational conditions on the predicted PFT force curves is evaluated. The input parameters employed for each of these sets of simulations are listed in Table 1.

Figure 5a,b shows that the adhesion force variation through H and z_0 mostly impacts the retraction segment of the $F-d$ curves while the approach segment and its slope remain almost unchanged. When the tip−surface adhesion is stronger, the "peeling off" process takes longer to complete, as the outermost regions of the contact zone become more resistant to detaching from the tip. For soft polymers, before tip−surface detachment during retraction, the surface can hold onto the retracting tip for a longer time and further deform above its undeformed state while the microcantilever deflects downward toward the sample. This results in a larger "pull-off" force during retraction. A final observation is that surface adhesion does not considerably affect the indentation depth.

Figure 5c−e depicts the $F-d$ curve variation due to changes of SLS parameters (eq 4) with a constant $\tau = 1$ μs, which is much smaller than the tip−surface interaction time. Either increasing E_0 when E_∞ is constant or decreasing E_∞ when E_0 is constant leads to force loops with greater hysteresis (Figure 5c,d). When τ is much less than the interaction time, most of the contact zone surface can transmit its stiffness from E_0 to E_∞ during the early periods of the contact time. Thus, the shape of the predicted $F-d$ curve for this τ configuration becomes more sensitive to E_∞ than E_0 variation. Therefore, while E_∞ reduction causes the whole force curve to change shape (Figure 5e), the slightly boosted dissipation due to E_0 increase manifests itself mainly in the attractive part of the retraction segment of the force curve (Figure 5d). However, when τ is much greater than the interaction time, this trend changes. In Figure 5e, we change both E_0 and E_∞ while their ratio E_∞/E_0 (Deborah number) remains constant. The resultant $F-d$ curve variation is a mixture of both effects seen when either E_0 or E_∞ changes.

Next, we examine the predicted $F-d$ curve variation due to changes of microcantilever properties, including microcantilever stiffness, k (Figure 5f) and tip radius, R (Figure 5g). The microcantilever deflection, q, proportionally changes with its k value variation, but the indentation depth, tip trajectory, and sample deformation during the interaction time do not noticeably change. When all of the parameters are identical except microcantilever stiffness, a softer microcantilever spends slightly more time interacting with the surface than a stiffer microcantilever, i.e., the interaction time is longer. That is because the snap-in/off with the surface for the softer microcantilever occurs earlier/later than a stiffer one. The snap-in/off phenomena are the results of the mutual contribution of the surface and the microcantilever to minimize the interaction energy between the approaching/retracting tip and the surface. The level of contribution of the surface and microcantilever in these unstable processes

https://doi.org/10.1021/acs.macromol.2c00147
Macromolecules 2022, 55, 8731−8740

depends on the surface/microcantilever properties and the adhesion force between them. Variation of the microcantilever's tip radius, R, does not noticeably influence the length of the interaction time, and its effect on the predicted $F-d$ curves is mainly due to an increase in the contact radius (Figure 5g). This leads to a slight decrease in indentation depth and an increase in pull-off force as tip radius increases. When the τ to interaction time ratio is smaller than 1, A_z (Figure 5h,i) reduction leads to less dissipative $F-d$ loops. This trend is reversed when the τ to interaction time ratio is greater than 1.

Inverse Problem. The inverse problem is to predict the properties of the surface based on the observed PFT AFM force curves and the AFM operating conditions. However, solving the inverse problem when the tip−surface interaction is modeled using EAM is not straightforward. As mentioned before, the challenge is partially due to the way the tip−surface interaction force is calculated by EAM. At each timestep of the interaction cycle, EAM first predicts the deformed surface profile and then calculates total F_{ts} by integrating tip−surface forces over the whole computational domain. This indirect link between tip position/velocity and the associated F_{ts} complicates the inverse solution. Therefore, we have utilized ML models as an alternative way to link PFT AFM force curves to the local viscoelastic and adhesive properties of the surface without requiring an analytical closed-form solution. The flowchart of the employed method is shown in Figure 6.

In material science, data analytics strategies are efficient and accurate methods to predict a material's characteristics, response, or behavior. The resultant surrogate ML models provide predictive capabilities based on recognizing the underlying patterns in past data. Specifically, when there is not an established theoretical model to connect the observables to the material characteristics and performing traditional computational or experimental measurements is hard, data-centric informatics methods are favorable.[24] These methods typically involve a "descriptor" selection phase in which the proper number of observables as input parameters of the model are carefully chosen. When the selected descriptors have different units or scales, implementing a scaling process to assimilate their scales is recommended. Then, a learning algorithm that connects the descriptors and the material properties of interest is established using a linear[25] or nonlinear regression-based technique such as support vector regression (SVR),[26] random forest regression (RFR),[27] or multilayer neural networks (MLP).[28] We need to have an inclusive set of material characteristics with known associated descriptors to train the predictive machine learning algorithm. Usually, different combinations of selected descriptors and various learning algorithms are examined to determine the configuration that delivers the optimized predictive performance.

The forward EAM-based algorithm predicts PFT force curves based on known material properties, microcantilever properties, and PFT operational parameters. We can utilize these predictions to build the required training data set for the inverse problem ML model, which is expected to map the problem descriptors: the given Force curve, the utilized microcantilever properties, and PFT operational parameters, to the material's viscoelastic and adhesive properties. Due to the following reasons, we utilize $F_{ts}(t)$ vs time ($F-t$ curves) as the model descriptor. First, the $F-t$ curve fulfills the mathematical function definition so that each member of the input set (domain) is mapped to exactly one object in the set of outputs (codomain). Second, $F-t$ curves (in contrast with $F-d$ curves) differentiate the approach and retraction phases of the force curve. Figure 7 shows an experimental $F-t$ curve

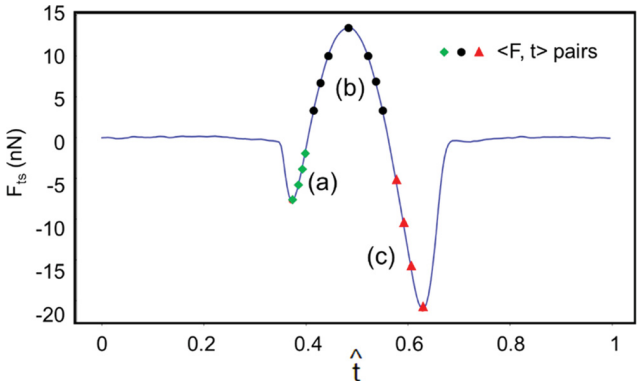

Figure 7. $F-t$ curve parametrization method. The dots shown on the curve are the 15 representative $\langle F, t\rangle$ pairs for the stable regions of an $F-t$ curve acquired on a polyolefin-based elastomer (ENGAGE 8003 Polyolefin Elastomer, Trademark of the Dow Chemical Company). The time is nondimensionalized based on the time period of the oscillation. The attractive-approach, repulsive, and attractive-retraction parts of the force curve are labeled as (a), (b), and (c), respectively.

from a polyolefin-based elastomer sample. The generated training data set is split into two portions: a training set and a test set. We use these sets to train and evaluate the predictive performance of the employed ML algorithm.

The $F-t$ curves need to be parametrized to a set of representative values acting as ML model descriptors. To proceed, we split the $F-t$ curve into three segments, as illustrated in Figure 7. The three segments are (a): Approach/attractive, (b): repulsive, and (c): retraction/attractive. First, the maximum tip−surface interaction force magnitude and its associated nondimensionalized time instance for each segment are determined: $\langle |F|_{max,\gamma}, t_{max,\gamma} \times f\rangle$ where γ: a, b, and c. Next, 12 $\langle F, t\rangle$ pairs on the stable parts of the given $F-t$ curve are recorded: $\langle \theta_i \times |F|_{max,\gamma}, t_{i,\gamma} \times f\rangle$ where: i: 1, 2, 3, θ_i:0.75, 0.5, 0.25, and γ: a, b, c. Each θ_i when $\gamma = b$ has two associated nondimensionalized time instances. Using this method, the stable parts of a given $F-t$ curve can be represented by 15 $\langle F, t\rangle$ data pairs with a total of 18 independent values which are: $\{|F|_{max,\gamma}, t_{i,\gamma} \times f\}$ where: i: 1, 2, 3 and γ: a, b, c. These 18 values, along with the tip radius, R, and microcantilever stiffness, k, constitute a large array of single-valued features which is used as the input of the machine learning algorithm. The employed operational parameters used for simulation and experiments are identical (ω_z = 2 kHz and a 10 nN peak force trigger), and therefore, they are not counted in the list of descriptors.

The forward solution algorithm generates a set of predicted $F-t$ curves for an associated known operational condition, microcantilever parameters, and sample viscoelastic/adhesive properties. For these simulations, we assume A_z = 50 nm, ω_z = 2 kHz, z_0 = 0.3 nm, ν = 0.5, and τ = 5 μs. The defined ranges for Z and other material/ microcantilever parameters for the training set simulations are shown in Table 2. These ranges are defined based on the expected properties for the elastomer samples and Bruker RTESPA-150-30 probes. The input parameters for the training set simulation are randomly selected over these defined ranges using the Latin hypercube sampling (LHS) method.[29] We selected the multilayer neural network (MLP)[28] algorithm to connect the model descriptors

https://doi.org/10.1021/acs.macromol.2c00147
Macromolecules 2022, 55, 8731−8740

Table 2. Ranges for Z and Other Material/Microcantilever Parameters for the Training Set Simulations[a]

R (nm)	k (N/m)	Z (nm)	E_0 (GPa)	E_∞ (GPa)	H ($\times 10^{-20}$ J)
30 ± 10	5 ± 2	42 ± 4	4.5 ± 4	0.11 ± 0.09	20 ± 15

[a]These ranges are defined based on the expected properties for elastomer samples and Bruker RTESPA-150-30 probes. The input parameters for the training set simulation are randomly selected over these defined ranges using the Latin hypercube sampling (LHS) method.[29]

to the output parameters: E_∞, E_0, H, and Z. We tried to solve this problem using MLP, LinearSVR, linear regression, and RFR and observed that MLP provides the most optimized predictivity performance and leads to fewer outliers on the test data. A grid-based search and k-fold cross-validation technique[30] are used to optimize the hyperparameters such as the size of the MLP hidden layers and to avoid overfitting the employed regression algorithms to the training data.[31] In the k-fold cross-validation technique, first, the training data set is divided into k portions, with an almost identical number of samples, and then the predictive performance of the algorithm is evaluated k times (k = 5 for this work). At each of these k times, one of the k portions of the data set is considered as the test set, and the remaining k-1 portions are used to train the algorithm. The optimal hyperparameters are the ones that deliver the minimum cross-validation error. Since the descriptors and output parameters are in various scales and different units and to reduce the impact of outliers, we scaled the training data parameters using a robust nonlinear preprocessing technique (Quantile Transformer) so that each follows a normal distribution. We calculated the error of the model predictions using the "mean absolute percentage error" (MAPE), which is defined as

$$\text{MAPE} = \frac{100\%}{n}\sum_{t=1}^{n}\left|\frac{A_t - P_t}{A_t}\right| \quad (6)$$

where n is the number of the predictions and A_t and P_t are the actual and the ML prediction values, respectively.

A typical set of predictive accuracy evaluation charts for the MLP model is illustrated in Figure 8. In each of these charts, the actual and predicted values, which are ideally equal, are compared for the employed ML models. We tested the predictive performance of the ML model by applying it to the prepared training data. For these performance test runs, 20% of the training data set is randomly selected as the test set, and the model is trained with the rest of the data. We repeated this process 10 times for each of the output parameters. The calculated MAPE for each of the parameters is listed in Table 3

Except for E_0, the MLP model provides acceptable (<10% error) predictive accuracy for other parameters. We hypothesize that the weaker predictive performance for E_0 is due to the reduced sensitivity of the simulated F–t curves to their associated E_0 values for the employed τ. This causes the pattern recognition process by the ML model to become insensitive. The selection of the single τ to interaction time ratio regulates the influence level of E_0 and E_∞ values on the resultant F–t curves when using the SLS viscoelasticity element. Nonetheless, the acceptable accuracy of the models' predictions for Z, E_∞, and H is promising.

Experimental Tests of the Surrogate Model. The developed ML algorithm is utilized on experimental PFT AFM

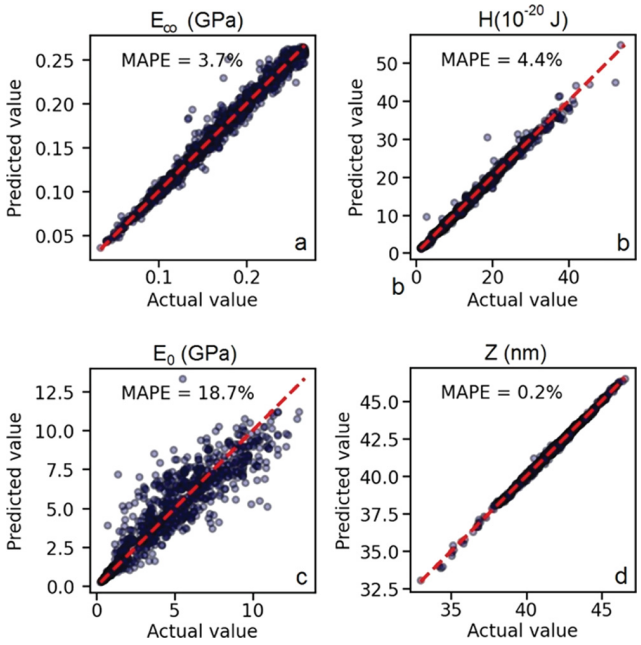

Figure 8. Typical set of the models' predictive accuracy evaluation charts when 20% of the training data is considered as test data. In these charts, the actual and predicted values, which are ideally supposed to be equal (represented as dashed red lines) for E_∞, E_0, H, and Z using each of the employed ML models are illustrated and compared.

Table 3. Calculated Mean Absolute Percentage Error (MAPE) of the Predictions by the Trained ML Algorithm[a]

	E_∞	E_0	H	Z
MLP	4.3 ± 0.4%	28.4 ± 6.5%	5.2 ± 0.6%	0.3 ± 0.1%

[a]These values are determined based on the calculated MAPEs of 10 times deploying the predictive model on the training data. The employed test data used for these evaluations is 20% of the whole training set and is randomly selected.

data on commercial elastomer samples. Three commercial grades of elastomers (ENGAGE 8003, 8100, and 8540 Polyolefin Elastomers from the Dow Chemical Company) were selected to represent a range of bulk mechanical properties.[32] For the experiments, approximately 300 nm thin sections were prepared using cryomicrotomy (Leica UC7 ultramicrotome, −120 °C) and placed onto cleaved mica substrates. PFT AFM was obtained on a Bruker MultiMode 8 AFM with a Nanoscope V controller running v9.40 NanoScope software. The experiment was run in QNM mode (quantitative nanomechanics) using a precalibrated probe (RTESPA-150-30 silicon microcantilever with a spring constant and tip radius of 6.25 N/m and 32 nm, respectively). Data were acquired at a tip oscillation frequency of 2 kHz and a 10 nN peak force trigger, with a force curve captured at each pixel in a 64 × 64 array. For each elastomer, a set of data was acquired with different peak force amplitudes (50, 75, or 100 nm). Typical PFT AFM F–t curves and their parametrization are shown in Figure 9. PFT AFM force curves are acquired as 64 × 64 arrays over 1 μm × 1 μm regions.

The samples' viscoelastic and adhesive property estimation using the trained ML algorithm are provided in Table 4. In Figure 10, we compare the moduli predictions from the ML analysis of the PFT data to moduli estimations from fitting the

https://doi.org/10.1021/acs.macromol.2c00147
Macromolecules 2022, 55, 8731−8740

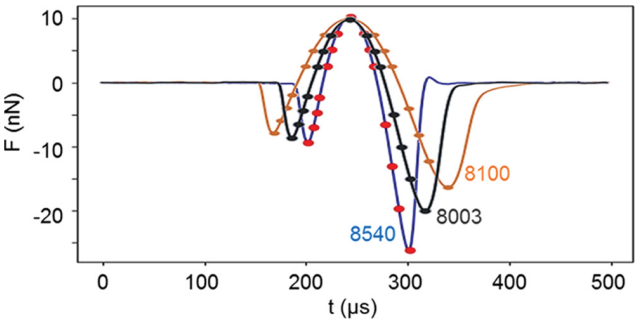

Figure 9. Typical PFT AFM $F-t$ curves acquired on elastomer ENGAGE 8100, 8003, and 8540 Polyolefin Elastomer samples and their parametrization. For the same PFT AFM operational conditions and microcantilever properties, the contact time increases when the sample is softer.

Table 4. Mean and Standard Deviation of Estimations for Viscoelastic and Adhesive Properties of Three Assessed Elastomer Grades by the Trained ML Algorithm[a]

	8100	8003	8540
E_∞ (MPa)	25.4 ± 0.0	32.1 ± 1.9	106.7 ± 24.8
E_0 (MPa)	268 ± 20.3	323.8 ± 29.7	565.4 ± 229.2
H (10^{-20} J)	18.0 ± 0.3	20.4 ± 0.8	22.6 ± 3.6
Z (nm)	35.3 ± 0.4	40.7 ± 0.2	44.0 ± 0.6

[a]These estimations are made based on deploying the ML algorithm on 128 acquired $F-t$ curves on 128 points on the sample's surface. The microcantilever and operational conditions are: k = 6.25 N/m, R = 32 nm, A_z = 50 nm, and f_z = 2 kHz. The amount of penetration for each sample can be estimated based on the calculated Z's (indentation = $Z - A_z + k F_{SP}$, where F_{SP} is the defined peak force trigger). τ = 5 μs based on the employed ω_Z = 2 kHz.

unloading curves of PFT and force volume mapping (FVM) JKR model.[22] The PFT curves are acquired at a rate of 2 kHz, while the FVM curves are acquired at a rate of 1 Hz. The ML predictions for E_0, which represent the modulus of the sample for greater than 2 kHz frequencies, are noticeably larger than E_{PFT}. Since the ML predictions were based on force curves acquired at 2 kHz, we expected $E_0 \gg E_{PFT}$. The ML predictions for E_{inf}, which represent the modulus of the sample for lower than 2 kHz frequencies, are relatively closer to E_{FVM}. This is also expected, given the differences in the interaction time between FVM and PFT. In general, these results illustrate the importance of considering a material's full viscoelastic properties when extracting modulus values.

CONCLUSIONS

We demonstrate the utilization of EAM as a rigorous three-dimensional viscoelastic contact model to simulate PFT AFM on soft polymeric samples. Analysis of the results enables a better understanding of the mutual interaction between the microcantilever and the surface during a PFT cycle. The results highlight the effects of viscoelasticity and long-range surface forces and can rigorously capture complex dynamics such as sample necking and adhesion-related energy loss due to peeling of the surface from the retracting tip. The computational parametric study depicts the role of sample properties, microcantilever properties, and PFT operational parameters on the predicted force curves. Since the developed algorithm does not lead to a straightforward way to relate the material viscoelasticity and adhesion characteristics to the PFT AFM

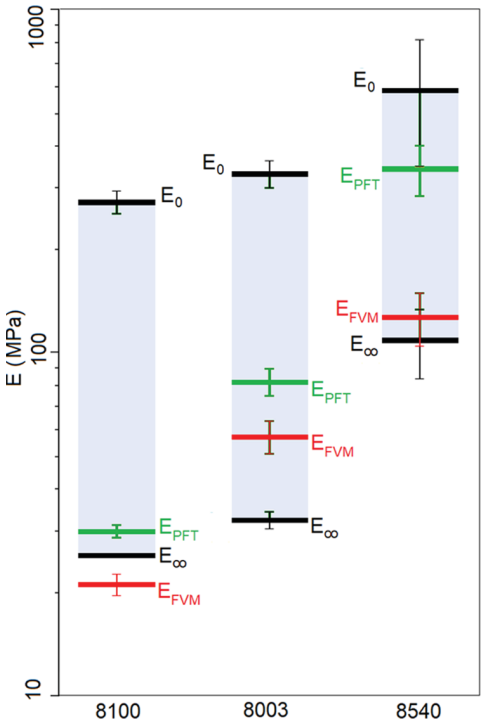

Figure 10. Moduli predictions from the ML analysis of the PFT data and moduli estimations from fitting the PFT and FVM force curves with the JKR model.[22] The PFT and FVM curves are acquired at 2 kHz and 1 Hz frequencies, respectively. The ML analysis is done using the PFT force–time curves (2 kHz).

observables, we instead employed data analytics approaches. We developed a multilayer neural network model, which provides the most optimized predictivity performance and leads to fewer outliers on the test data. The required labeled data to train and evaluate the ML model performance is prepared using the developed validated algorithm for the forward solution. Using the trained ML algorithm on the experimental PFT AFM data acquired on three commercial grades of elastomers results in physically acceptable predictions for surface viscoelastic and adhesion properties.

ASSOCIATED CONTENT

Supporting Information

The Supporting Information is available free of charge at https://pubs.acs.org/doi/10.1021/acs.macromol.2c00147.

The calculation method for the tip–surface interaction force in eq 3, $F_{ts}(t)$ (PDF)

AUTHOR INFORMATION

Corresponding Author

Arvind Raman − *School of Mechanical Engineering, Purdue University, West Lafayette, Indiana 47907, United States; Birck Nanotechnology Center, West Lafayette, Indiana 47907, United States;* orcid.org/0000-0001-6297-5581; Email: raman@purdue.edu

Authors

Bahram Rajabifar − *School of Mechanical Engineering, Purdue University, West Lafayette, Indiana 47907, United States; Birck Nanotechnology Center, West Lafayette, Indiana 47907, United States;* orcid.org/0000-0002-4866-8339

https://doi.org/10.1021/acs.macromol.2c00147
Macromolecules 2022, 55, 8731−8740

Gregory F. Meyers − *Analytical Sciences, The Dow Chemical Company, Midland, Michigan 48667, United States*
Ryan Wagner − *School of Mechanical Engineering, Purdue University, West Lafayette, Indiana 47907, United States; Birck Nanotechnology Center, West Lafayette, Indiana 47907, United States;* orcid.org/0000-0002-4111-8027

Complete contact information is available at: https://pubs.acs.org/10.1021/acs.macromol.2c00147

Notes

The authors declare no competing financial interest.

REFERENCES

(1) Garcia, R. Nanomechanical mapping of soft materials with the atomic force microscope: methods, theory and applications. *Chem. Soc. Rev.* **2020**, *49*, 5850−5884.
(2) Butt, H.-J.; Cappella, B.; Kappl, M. Force measurements with the atomic force microscope: Technique, interpretation and applications. *Surf. Sci. Rep.* **2005**, *59*, 1−152.
(3) Hurley, D. C.; Campbell, S.; Killgore, J.; Cox, L.; Ding, Y. Measurement of Viscoelastic Loss Tangent with Contact Resonance Modes of Atomic Force Microscopy. *Macromolecules* **2013**, *46*, 9396−9402.
(4) Yablon, D. G.; Gannepalli, A.; Proksch, R.; Killgore, J.; Hurley, D. C.; Grabowski, J.; Tsou, A. H. Quantitative Viscoelastic Mapping of Polyolefin Blends with Contact Resonance Atomic Force Microscopy. *Macromolecules* **2012**, *45*, 4363−4370.
(5) Killgore, J. P.; Hurley, D. C. Pulsed contact resonance for atomic force microscopy nanomechanical measurements. *Appl. Phys. Lett.* **2012**, *100*, No. 053104.
(6) Rajabifar, B.; Bajaj, A. K.; Reifenberger, R. G.; Proksch, R.; Raman, A. Discrimination of Adhesion and Viscoelasticity from Nanoscale Maps of Polymer Surfaces using Bimodal Atomic Force Microscopy. *Nanoscale* **2021**, *13*, 17428.
(7) Pittenger, B.; Erina, N.; Su, C. Quantitative mechanical property mapping at the nanoscale with Peak Force QNM. *Veeco Appl. Note A* **2010**, *128*, 1−12.
(8) Chopinet, L.; Formosa, C.; Rols, M.; Duval, R.; Dague, E. Imaging living cells surface and quantifying its properties at high resolution using AFM in QI mode. *Micron* **2013**, *48*, 26−33.
(9) Garcıa, R.; Perez, R. Dynamic atomic force microscopy methods. *Surf. Sci. Rep.* **2002**, *47*, 197−301.
(10) Efremov, Y. M.; Shpichka, A.; Kotova, S.; Timashev, P. Viscoelastic mapping of cells based on fast force volume and PeakForce Tapping. *Soft Matter* **2019**, *15*, 5455−5463.
(11) Pittenger, B.; Erina, N.; Su, C. *Quantitative Mechanical Property Mapping at the Nanoscale with PeakForce QNM*; Application Note Veeco Instruments Inc, 2010; Vol. *1*.
(12) Kékicheff, P.; Contal, C. Cationic-Surfactant-Coated Mica Surfaces below the Critical Micellar Concentration: 1. Patchy Structures As Revealed by Peak Force Tapping AFM Mode. *Langmuir* **2019**, *35*, 3087−3107.
(13) Amo, C. A.; Garcia, R. Fundamental high-speed limits in single-molecule, single-cell, and nanoscale force spectroscopies. *ACS Nano* **2016**, *10*, 7117−7124.
(14) Dokukin, M. E.; Sokolov, I. Nanoscale compositional mapping of cells, tissues, and polymers with ringing mode of atomic force microscopy. *Sci. Rep.* **2017**, *7*, No. 11828.
(15) Rajabifar, B.; Jadhav, J. M.; Kiracofe, D.; Meyers, G. F.; Raman, A. Dynamic AFM on Viscoelastic Polymer Samples with Surface Forces. *Macromolecules* **2018**, *51*, 9649−9661.
(16) Hertz, H. Über die Berührung fester elastischer Körper. *J. Reine Angew. Math.* **1882**, *92*, 156−171.
(17) Ting, T. C. T. The contact stresses between a rigid indenter and a viscoelastic half-space. *J. Appl. Mech.* **1966**, *33*, 845−854.
(18) Lee, E. H.; Radok, J. R. M. The contact problem for viscoelastic bodies. *J. Appl. Mech.* **1960**, *27*, 438−444.
(19) Attard, P. Interaction and deformation of elastic bodies: origin of adhesion hysteresis. *J. Phys. Chem. B* **2000**, *104*, 10635−10641.
(20) Attard, P. Interaction and deformation of viscoelastic particles. 2. Adhesive particles. *Langmuir* **2001**, *17*, 4322−4328.
(21) Rajabifar, B.; Wagner, R.; Raman, A. A fast first-principles approach to model atomic force microscopy on soft, adhesive, and viscoelastic surfaces. *Mater. Res. Express* **2021**, *8*, No. 095304.
(22) Johnson, K.; Kendall, K.; Roberts, A. In *Surface Energy and the Contact of Elastic Solids*, Proceedings of the Royal Society of London A: Mathematical, Physical and Engineering Sciences, The Royal Society, 1971; pp 301−313.
(23) Derjaguin, B. V.; Muller, V. M.; Toporov, Y. P. Effect of contact deformations on the adhesion of particles. *J. Colloid Interface Sci.* **1975**, *53*, 314−326.
(24) Ramprasad, R.; Batra, R.; Pilania, G.; Mannodi-Kanakkithodi, A.; Kim, C. Machine learning in materials informatics: recent applications and prospects. *npj Comput. Mater.* **2017**, *3*, No. 54.
(25) Kim, C.; Pilania, G.; Ramprasad, R. From organized high-throughput data to phenomenological theory using machine learning: the example of dielectric breakdown. *Chem. Mater.* **2016**, *28*, 1304−1311.
(26) Smola, A. J.; Schölkopf, B. A tutorial on support vector regression. *Stat. Comput.* **2004**, *14*, 199−222.
(27) Liaw, A.; Wiener, M. Classification and regression by randomForest. *R News* **2002**, *2*, 18−22.
(28) Sarle, W. S. *Neural Networks and Statistical Models*, 1994.
(29) McKay, M. D.; Beckman, R. J.; Conover, W. J. A comparison of three methods for selecting values of input variables in the analysis of output from a computer code. *Technometrics* **2000**, *42*, 55−61.
(30) Bergstra, J.; Bengio, Y. Random search for hyper-parameter optimization. *J. Mach. Learn. Res.* **2012**, *13*, 281−305.
(31) James, G.; Witten, D.; Hastie, T.; Tibshirani, R. *An Introduction to Statistical Learning*, Springer, 2013; Vol. *112*.
(32) The Dow Chemical Company, Engage Polyolefin Elastomers Product Selection Guide, Form No. 777-088-01E-0819, 2019.